Coriolis force induced topological order for classical mechanical vibrations

Wang, Yao-ting; Luan, Pi-gang; Zhang, Shuang

DOI:
10.1088/1367-2630/17/7/073031

Document Version
Publisher's PDF, also known as Version of record

Citation for published version (Harvard):
Wang, Y, Luan, P & Zhang, S 2015, 'Coriolis force induced topological order for classical mechanical vibrations', *New Journal of Physics*, vol. 17, no. 7, 073031. https://doi.org/10.1088/1367-2630/17/7/073031

Coriolis force induced topological order for classical mechanical vibrations

2015 New J. Phys. 17 073031

(http://iopscience.iop.org/1367-2630/17/7/073031)

New Journal of Physics
The open access journal at the forefront of physics

Deutsche Physikalische Gesellschaft DPG
IOP Institute of Physics

Published in partnership with: Deutsche Physikalische Gesellschaft and the Institute of Physics

OPEN ACCESS

RECEIVED
16 March 2015

REVISED
29 May 2015

ACCEPTED FOR PUBLICATION
23 June 2015

PUBLISHED
31 July 2015

PAPER

Coriolis force induced topological order for classical mechanical vibrations

Yao-Ting Wang[1], **Pi-Gang Luan**[2] **and Shuang Zhang**[1,3]

[1] School of Physics and Astronomy, University of Birmingham, Birmingham B15 2TT, UK
[2] Department of Optics and Photonics, National Central University, Jhongli 32001, Taiwan
[3] Author to whom any correspondence should be addressed.

E-mail: s.zhang@bham.ac.uk

Keywords: topological order, vibration, crystal

Abstract

We show that topological order and vibrational edge modes can exist in a classical mechanical system consisting of a two-dimensional honeycomb lattice of masses and springs. The band structure shows the existence of Dirac cones and unconventional edge states that are similar to the vibrational modes in graphene. Interestingly, as the system is placed on a constantly rotational coordinate system, the Coriolis force resulting from the non-inertial reference frame introduces time-reversal symmetry breaking and leads to topologically nontrivial band gaps. The nontrivial topological orders are further verified by the calculation of Chern numbers for corresponding bands.

Over the past few decades, the discovery of matter with topological nature, such as quantum Hall effect and topological insulators, has attracted much attention towards these novel phenomena [1–5]. Topological protection, the immunity against scattering of matter waves by disorder, is a main property existing in these kinds of materials. The scattering-immunity states probably are the most impressive concept of these materials because this robustness of electronic waves was previously only known in superconductors. Theoretical studies show that breaking time-reversal symmetry plays a crucial role in opening a nontrivial frequency gap, which is an essential condition to bring about the topologically protected edge states [6]. The condition of time-reversal symmetry breaking can be fulfilled through applying an external magnetic field, or the intrinsic spin–orbit coupling of the material itself. Recently, the thriving progress of topological properties in condensed matter has also led to a great interest in discovering similar phenomenon in other physics systems. Raghu and Haldane [7, 8] proposed that the optical analog of quantum Hall effect could be achieved by using periodically arranged gyromagnetic rods. Their idea implies that the nontrivial topological phase is fundamentally a wave phenomenon rather than quantum effect. Following this concept, many research groups have realized topologically protected one-way edge states theoretically [8–10] and experimentally in photonic systems [11]. Also, by employing periodically arranged meta-crystals and helical arrays, two approaches of photonic analog are proposed to realize a photonic topological insulator that breaks time-reversal symmetry for each spin but preserves it in the whole system [12, 13]. A few recent works focus on the analogs of quantum Hall effect in acoustic or phononic systems [14–17]. Here, we show that a classical mass-spring crystal in a rotating frame can possess the topologically protected edge modes of classical vibration under the influence of the Coriolis force.

We begin by considering a two-dimensional spring-mass system with honeycomb lattice in the inertial lab frame. The system consists of a series of honeycomb-arranged rigid body spheres with mass M and massless springs with elastic constant C, as shown in figures 1(a) and (b). Let a be the separation between the nearest-neighbor spheres (A and B) and the lattice translation vectors are expressed as $\mathbf{r}_{mn} = m\mathbf{a}_1 + n\mathbf{a}_2$ with $\mathbf{a}_1 = \sqrt{3}a\,\hat{\mathbf{x}}$, $\mathbf{a}_2 = \left(\sqrt{3}\hat{\mathbf{x}} + 3\hat{\mathbf{y}}\right)a/2$. The three vectors connecting a sphere A to the nearest-neighbor spheres are

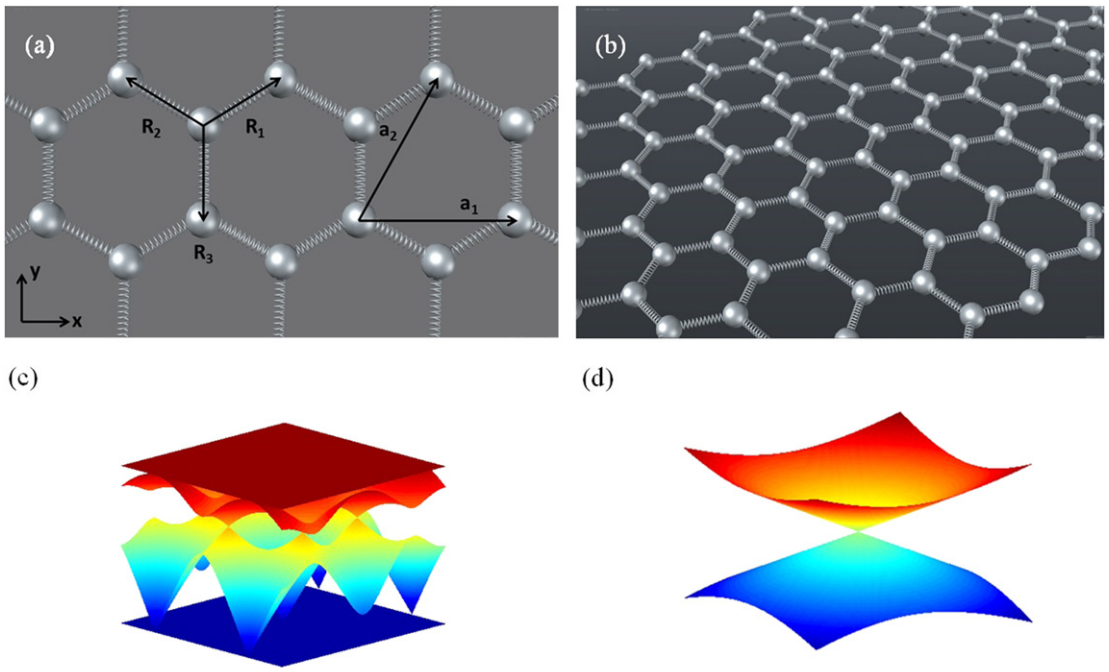

Figure 1. (a) Top view of our model made by soft springs and rigid particles. (b) A three-dimensional plot of the semi-infinite mass-spring ribbon ending with zigzag edges. (c) The band structure of two-dimensional mass-spring model with honeycomb lattice and (d) a zoomed-in figure of Dirac cone in the vicinity of a certain K point with mass and elastic constant equals to ten grams and 4 N m^{-1}, respectively.

$$\begin{aligned}\mathbf{R}_1 &= \frac{1}{3}\left(\mathbf{a}_1 + \mathbf{a}_2\right)\\ &= \frac{a\sqrt{3}}{2}\hat{\mathbf{x}} + \frac{a}{2}\hat{\mathbf{y}}\\ \mathbf{R}_2 &= \frac{1}{3}\left(-2\mathbf{a}_1 + \mathbf{a}_2\right)\\ &= -\frac{a\sqrt{3}}{2}\hat{\mathbf{x}} + \frac{a}{2}\hat{\mathbf{y}}\\ \mathbf{R}_3 &= \frac{1}{3}\left(\mathbf{a}_1 - 2\mathbf{a}_2\right)\\ &= -a\hat{\mathbf{y}}.\end{aligned}$$

Let displacements of the A and B spheres be $\boldsymbol{\xi}$ and $\boldsymbol{\eta}$, respectively, the difference between them be $\mathbf{u}$, and the dynamic displacement of longitudinal oscillation between the two spheres is expressed as $\mathbf{R}' = \mathbf{R} + \mathbf{u}$, with $|\mathbf{R}'| = \sqrt{|\mathbf{R}|^2 + 2\mathbf{R}\cdot\mathbf{u} + |\mathbf{u}|^2} \approx |\mathbf{R}| + \hat{\mathbf{R}}\cdot\mathbf{u}$ (a vector with hat represents an unit vector). Hence, the variation in length of the spring connecting the two spheres is $\Delta_R = \hat{\mathbf{R}}\cdot\mathbf{u}$.

According to the preceding description, if we assume the general form $\boldsymbol{\xi}(m, n) = \boldsymbol{\xi}\, p^m s^n e^{-i\omega t}$, $\boldsymbol{\eta}(m, n) = \boldsymbol{\eta}\, p^m s^n e^{-i\omega t}$, the systematic equations of dispersion relation are expressed as [19]

$$\begin{aligned}\omega^2\boldsymbol{\xi} = \omega_0^2\Big[&\hat{\mathbf{R}}_1\hat{\mathbf{R}}_1\cdot(\boldsymbol{\xi} - \boldsymbol{\eta})\\ &+ \hat{\mathbf{R}}_2\hat{\mathbf{R}}_2\cdot(\boldsymbol{\xi} - p^*\boldsymbol{\eta}) + \hat{\mathbf{R}}_3\hat{\mathbf{R}}_3\cdot(\boldsymbol{\xi} - s^*\boldsymbol{\eta})\Big],\end{aligned} \tag{1a}$$

$$\begin{aligned}\omega^2\boldsymbol{\eta} = \omega_0^2\Big[&\hat{\mathbf{R}}_1\hat{\mathbf{R}}_1\cdot(\boldsymbol{\eta} - \boldsymbol{\xi})\\ &+ \hat{\mathbf{R}}_2\hat{\mathbf{R}}_2\cdot(\boldsymbol{\eta} - p\boldsymbol{\xi}) + \hat{\mathbf{R}}_3\hat{\mathbf{R}}_3\cdot(\boldsymbol{\eta} - s\boldsymbol{\xi})\Big].\end{aligned} \tag{1b}$$

where $p = e^{i\mathbf{k}\cdot\mathbf{a}_1}$, $s = e^{i\mathbf{k}\cdot\mathbf{a}_2}$, and $\omega_0^2 = C/M$ is the characteristic frequency of spring-mass system. By solving the eigenvalue problem $\mathbf{H}\mathbf{x} = \omega^2\mathbf{x}$ given by (1), we obtain four solutions, two of them are 0 and $\sqrt{3}\,\omega_0$, while the other two are described by the following dispersion relation

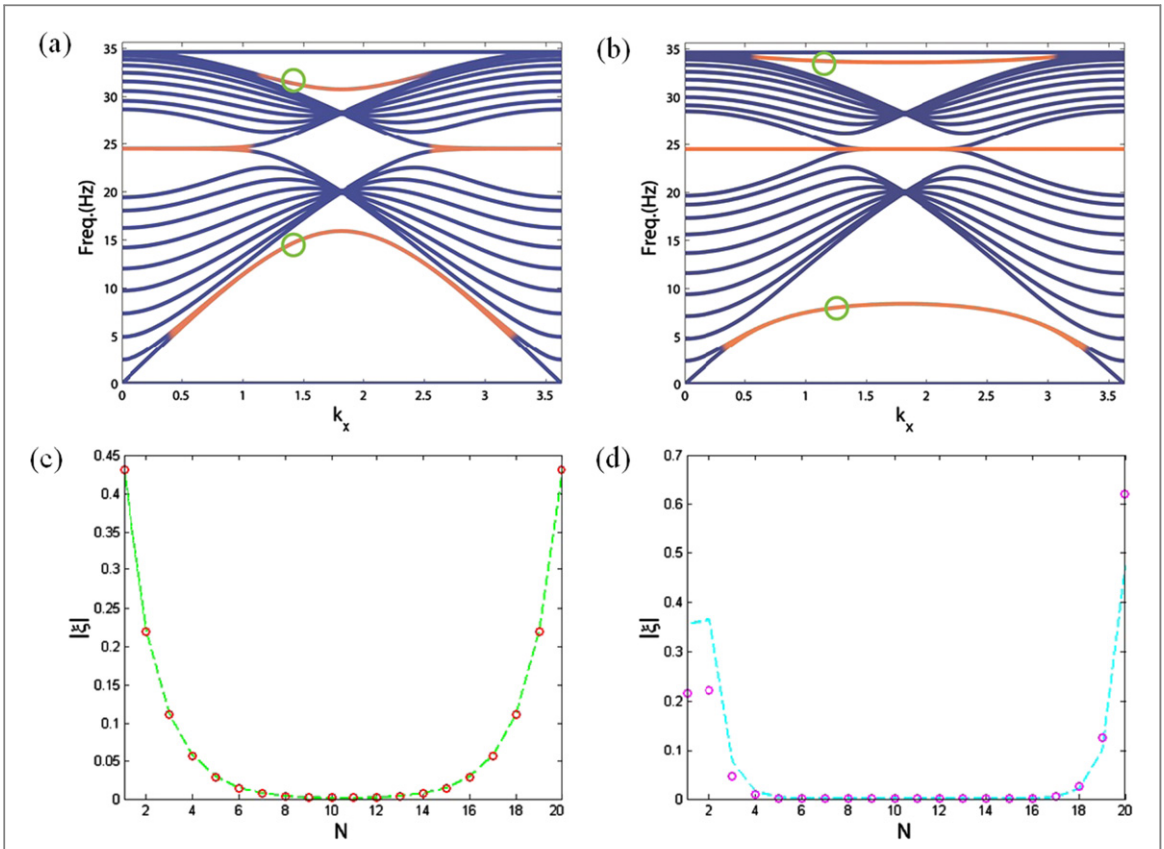

Figure 2. (a) The one-dimensional band diagram calculated from zigzag spring-mass ribbon. (b) One-dimensional band diagram for bearded edges. (c) Absolute value of amplitudes for zigzag edge modes, the green dashed line corresponds to the top edge state and the red circles are to the opposite one. (d) Its absolute value of amplitudes of figure 2(b) for both edge states.

$$\omega = \omega_0 \sqrt{\frac{3}{2} \pm \frac{1}{2} \sqrt{3 + 2\left\{\cos\left(\mathbf{k}\cdot\mathbf{a}_1\right) + \cos\left(\mathbf{k}\cdot\mathbf{a}_2\right) + \cos\left[\mathbf{k}\cdot\left(\mathbf{a}_1 - \mathbf{a}_2\right)\right]\right\}}}. \tag{2}$$

The band structure described by equation (2) is shown in figure 1(c). There exist four bands, with the two flat bands of transverse modes at zero frequency and $\sqrt{3}\,\omega_0$, and two dispersive longitudinal modes. The number of zero modes is given by the rank-nullity theorem, which can also be described by an index theorem proposed by Kane and Lubensky [17]. Physically, these two flat bands arise from the assumption of negligible transverse restoring force of the springs (see the appendix for detailed discussion). If the transverse restoring force is present in a similar way as in graphene, both the optical and acoustic transverse modes would become dispersive, as shown in [20]. Six linear degeneracies are seen in the vicinity of K points around the entire Brillouin zone. By expanding equation (2) to the second order at K point $\left(4\pi/3\sqrt{3}\,a,\ 0\right)$, we show that $\omega = \omega_0\,(1 \pm |\delta\mathbf{k}|\,a/4)$ is a linear function with respect to the $\mathbf{k}$ vector. Figure 1(d) indicates the zoomed-in plot near the K point. These degeneracies, referred to as Dirac points, provide the chance to exhibit topological edge states known as the integer quantum Hall effect when the time-reversal symmetry is broken.

To investigate the vibrational edge modes, we study an infinitely long ribbon along the *x* direction, but with a finite width containing *N* unit cells in the *y* direction. The band structure of a spring-mass ribbon with honeycomb lattice is shown in figure 2. Similar to a graphene ribbon ending with bearded edges, a flat edge state between two Dirac points is observed in the energy spectrum, shown in figures 2(a) and (b). Due to the existence of the flat energy band, at the corresponding frequency, the particles located on the edge vibrate locally without transporting energy forward. For the bearded edge, the band diagram shown in figure 2(b) also gives a flat band throughout the whole $\mathbf{k}$ space. We note that it differs from conventional bearded flat edge mode for electrons in graphene, which only appears in the region between the two K points. In addition, two unconventional edge modes (red curves) are found around the Dirac points in figures 2(a) and (b). These new modes for a beaded or zigzag boundary were recently proposed and observed by Plotnik *et al* in a photonic analog system of graphene

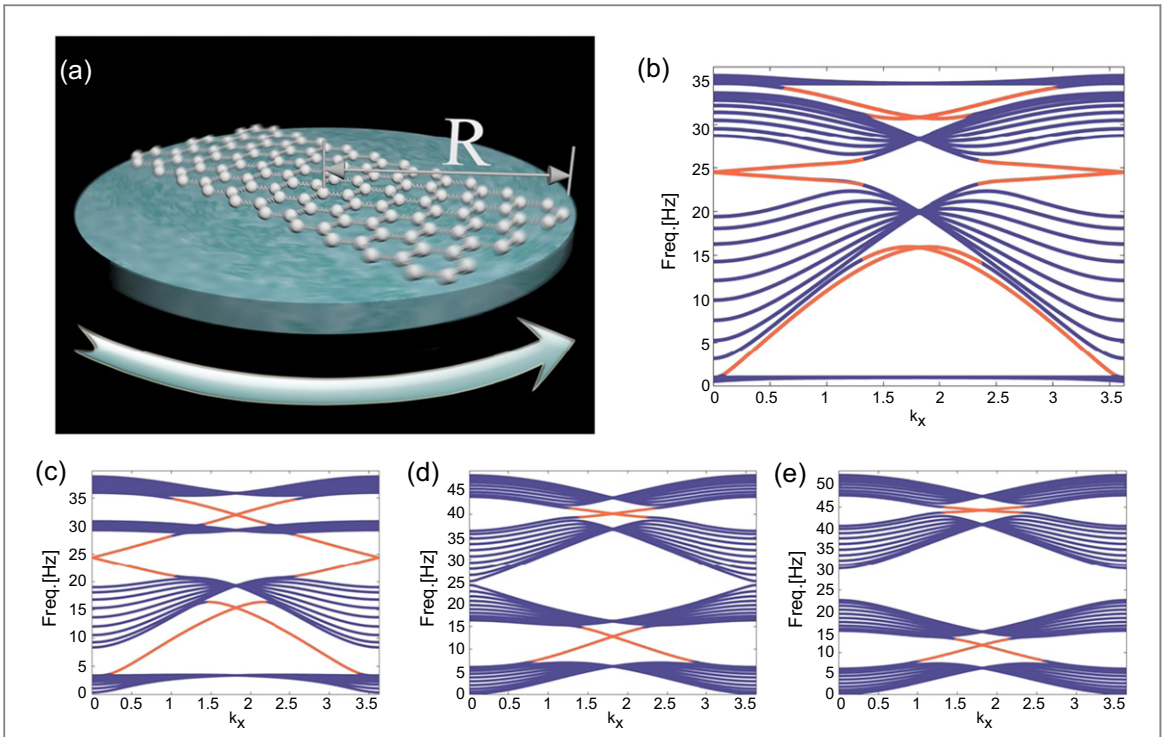

Figure 3. (a) A schematic diagram of the non-inertial system. One-dimensional band structure for a mass-spring ribbon end with zigzag boundary applied constantly angular velocity (b) $\boldsymbol{\Omega} = 1$, (c) $\boldsymbol{\Omega} = 4$, (d) $\boldsymbol{\Omega} = \boldsymbol{\Omega}_c$, and (e) $\boldsymbol{\Omega} = 15$ Hertz.

[21] and have been theoretically investigated for phonons in real graphene [22]. Figures 2(c) and (d) show the vibrational amplitudes at points A along the transverse cross-section (N = 20) of the spring-mass ribbon. As predicted by the energy spectrum, the peaks indicate that the vibration of particles is highly confined to the corresponding edge.

Next, we introduce time-reversal symmetry breaking by placing the spring-mass lattice in a rotating frame, as schematically shown in figure 3(a). In classical mechanics, objects moving in a rotating reference frame experience inertial forces—centrifugal force and Coriolis force—resulting in corrections to the equation of motion. For a particle oscillating harmonically on a counterclockwise rotating round plate with a constant angular velocity $\boldsymbol{\Omega}$ in the z direction, the Lagrangian in terms of equilibrium position r, elongation Δr, and vibration velocity v can be expressed as $L = \left[Mv^2 - C\Delta r^2 + M(\boldsymbol{\Omega} \times \mathbf{r})^2\right]/2 + M\mathbf{v} \cdot (\boldsymbol{\Omega} \times \mathbf{r})$ [23]. The first two terms correspond to the normal simple harmonic oscillation, the third term times −1 represents the elastic potential energy when the centrifugal force is present, and the fourth term corresponds to the Coriolis force. Then, except for the centrifugal term, by defining $\mathbf{A} = (\boldsymbol{\Omega} \times \mathbf{r})/2$ as an effective vector potential in the Coulomb gauge, the Lagrangian can be rewritten as $L = \left[Mv^2 - C\Delta r^2\right]/2 + 2M\mathbf{A} \cdot \mathbf{v}$, which describes the dynamics in a nonrotating frame with a constant magnetic field applied in the normal direction while the elastic constant is given as the corrected value, and the relevant 'charge' of the particle is Q = 2M, without any 'Coulomb interaction' between a pair of particles. On the other hand, the presence of centrifugal force will disturb the system and break the translational symmetry of the lattice. However, since the centrifugal force has a quadratic dependence on the angular frequency of the rotation frame, its effect can be neglected for sufficiently small angular frequencies. More detailed discussion of the effect of the centrifugal force will be given later. With only the Coriolis force taken into account, the dynamic equations for the propagating modes can be written as

$$\begin{aligned}\omega^2\boldsymbol{\xi} + 2i\omega\Omega\hat{\mathbf{z}} \times \boldsymbol{\xi} = \omega_0^2\Big[&\hat{\mathbf{R}}_1\hat{\mathbf{R}}_1 \cdot (\boldsymbol{\xi} - \boldsymbol{\eta}) \\ &+ \hat{\mathbf{R}}_2\hat{\mathbf{R}}_2 \cdot \left(\boldsymbol{\xi} - p^*\boldsymbol{\eta}\right) \\ &+ \hat{\mathbf{R}}_3\hat{\mathbf{R}}_3 \cdot \left(\boldsymbol{\xi} - s^*\boldsymbol{\eta}\right)\Big] \end{aligned} \tag{3a}$$

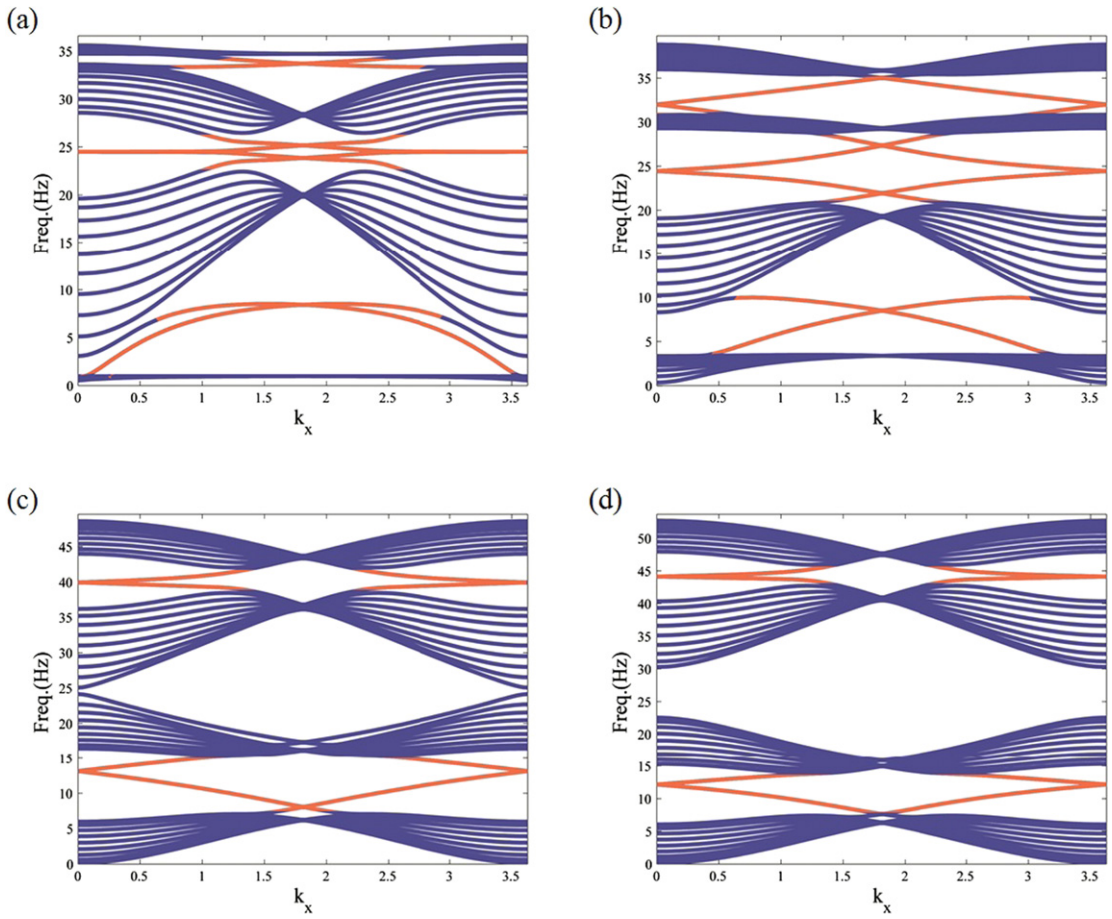

Figure 4. Frequency diagram in one dimension for a mass-spring ribbon end with bearded boundary applied constantly angular velocity at (a) $\boldsymbol{\Omega} = 1$, (b) $\boldsymbol{\Omega} = 4$, (c) $\boldsymbol{\Omega} = \boldsymbol{\Omega}_c$, and (d) $\boldsymbol{\Omega} = 15$ Hertz.

$$\omega^2\boldsymbol{\eta} + 2i\omega\Omega\hat{\mathbf{z}} \times \boldsymbol{\eta} = \omega_0^2\Big[\hat{\mathbf{R}}_1\hat{\mathbf{R}}_1 \cdot (\boldsymbol{\eta} - \boldsymbol{\xi}) + \hat{\mathbf{R}}_2\hat{\mathbf{R}}_2 \cdot (\boldsymbol{\eta} - p\boldsymbol{\xi}) + \hat{\mathbf{R}}_3\hat{\mathbf{R}}_3 \cdot (\boldsymbol{\eta} - s\boldsymbol{\xi})\Big]. \quad (3b)$$

The band structure can be obtained by solving the eigenvalue equation. For numerical simulations, hereafter we choose C = 4 N m^{-1} and M = 10 g. Figures 3(b)–(e) show the band structures at four different angular velocities of the rotation frame, $\boldsymbol{\Omega} = 1, 4, \boldsymbol{\Omega}_c$, and 15 Hz, respectively. At the lowest angular velocity $\boldsymbol{\Omega} = 1$ Hz, interestingly, the top and bottom bands evolve from the originally flat bands in the nonrotating frame to have finite bandwidth. All three band gaps between the four bands are topologically nontrivial because of time-reversal symmetry breaking, and there exist topologically protected edge modes within each bandgap, as shown in figure 3(b).

As the angular velocity increases to 4 Hz, the band gaps broaden and the dispersion of the edge modes become more linear. When the angular velocity reaches to $\Omega_c = \sqrt{3C/8M} \sim 12.247$ Hz, the second and third band touch each other and the gap between them is closed. When the angular velocity is further increased, the gap reopens but is now converted into a trivial one, which does not contain any edge modes due to the band crossing, as shown in figure 3(d). Figures 4(a)–(d) show the bearded edge modes under different speeds of rotation. Similar to the zigzag edge, the bearded edge modes exist in every band gap, as the angular velocity is less than $\boldsymbol{\Omega}_c$. Due to band inversion, topological phase transition occurs at the second and third bands after reaching the critical angular frequency.

We now address the influence of equilibrium position correction affected by centrifugal force. To estimate the effect of the centrifugal force, we consider a mass-spring ribbon with characteristic frequency $\omega_0 = 20$ Hz located on a round plate with a width of ten periods (N = 10), a length two times the width, and a lattice constant $a = \sqrt{3}$ cm. The center of the ribbon is located at the center of the round plate. Under the approximation

$\Omega^2 \ll \omega_0^2$, the new equilibrium position of each sphere is given by

$$\Delta \mathbf{a}_{mn}^{A,B} = \frac{2\Omega^2}{3\omega_0^2}\mathbf{r}_{mn}^{A,B}, \tag{4}$$

where $\mathbf{r}_{mn}^{A,B}$ are the position vectors for particle A and B relative to the center of the strip. For angular velocity $\boldsymbol{\Omega} = 2$ Hz, the farthest particle from the center is shifted from its static position by 0.129 cm due to the centrifugal force. It has been shown that the relation between disorder and deviation of band gap is linked by an approximate formula $\delta^2 \sim \Delta\omega/3\omega_{cen}$ or $\Delta\omega \sim 0.017\omega_{cen}$ [24], where δ is the deviation parameter defined as $\Delta a/a$, $\Delta\omega$ is the change of bandgap, and ω_{cen} gives the central frequency of a certain gap. The gap widths for each band are 2.12, 4.01, and 2.12 Hz and their corresponding $\Delta\omega$ are 0.05, 0.42, and 0.57 Hz, respectively. For this particular example, the change of bandgap is so small that it can be neglected while the rotating frequency is sufficiently low. Hence, as long as the angular velocity is much less than the characteristic frequency, the influence of equilibrium position shift is insignificant to the band structure. For operations at higher angular velocity, one can always set all particles at corrected positions in advance such that when a round plate rotates at certain angular velocity, all particles move back to the original ordered locations.

To confirm the topological order of edge modes, we have numerically evaluated the Chern number for each band. The formula for the Chern number is expressed as $C_n = (1/2\pi)\int_{BZ} \mathrm{d}^2\mathbf{k} \cdot \mathbf{F}_n$, where $\mathbf{F}_n = i\left\langle \nabla_{\mathbf{k}} n\right| \times \left|\nabla_{\mathbf{k}} n\right\rangle$ is the Berry curvature for the nth band, and the integration is taken throughout the first Brillouin zone. The result shows that, at $\boldsymbol{\Omega} = 4$ Hz, Chern numbers from the lowest to the highest band are given as $\{-1,\ 0,\ 0,\ 1\}$. It shows that the edge modes in each bandgap are topologically protected in association with a net change of Chern number $\Delta C = 2$. When $\boldsymbol{\Omega}$ reaches $\boldsymbol{\Omega}_c$, topological phase transition occurs so that the Chern numbers for bands become $\{-1,\ 1,\ -1,\ 1\}$. The system now exhibits topologically nontrivial Chern number difference $\Delta C = 2$ only in the first through second and third through fourth bands. The central band gap now becomes nontrivial, and there exist no scattering immune edge modes. The Chern number calculation agrees perfectly with the results shown in figures 3 and 4.

In summary, we have introduced a simple classical mechanical system—a honeycomb lattice plane consisting of rigid bodies and soft springs, which, when positioned in a rotating frame, can have nontrivial frequency gaps that give rise to topologically protected edge modes. Due to the simplicity of the system, these Coriolis-force-induced topological vibrational modes can be readily observed experimentally for low-frequency oscillations.

Acknowlegments

The work is supported in part by EPSRC. PGL would like to acknowledge the National Science Council of Taiwan (Grant No. NSC 101-2112-M-008 -015 -MY3, NSC 103-2918-I-008-012). YTW would like to thank the Ministry of Education, Taiwan for the financial support.

Appendix. A generalized model including the transverse restoring force

In the main text, we assume transverse restoring force is too weak to be considered. However, due to the centrifugal force, all the springs are stretched and transverse force becomes more and more crucial with the increase of angular frequency. In this appendix, we will include this term to investigate its effect. If the restoring force caused by stretching a spring is to be considered, the original elastic potential energy $\frac{C}{2}\left(\hat{\mathbf{R}} \cdot \mathbf{u}\right)^2$ should be replaced by

$$\begin{aligned}&\frac{C_L}{2}\left(\hat{\mathbf{R}} \cdot \mathbf{u}\right)^2 + \frac{C_T}{2}\left|\hat{\mathbf{R}} \times \mathbf{u}\right|^2 \\ &\quad = \frac{C_L - C_T}{2}\left(\hat{\mathbf{R}} \cdot \mathbf{u}\right)^2 + \frac{C_T}{2}|\mathbf{u}\ |^2.\end{aligned} \tag{A.1}$$

Note that we only consider in-plane transverse displacement here. For out-of-plane, transverse vibration can be decoupled from the in-plane vibration modes [19], and hence we will exclude it in the following discussion. The modified Lagrangian becomes

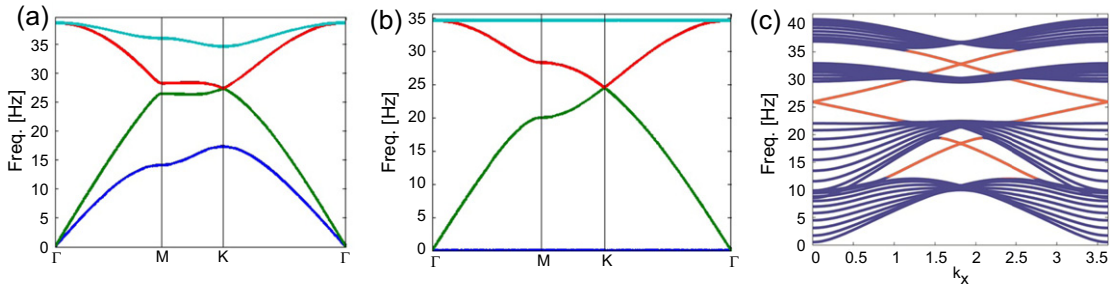

Figure A1. The band structure with different transverse constant (a) 1 (b) 0. Red and green line denote optical and acoustic longitudinal modes, respectively; light blue and blue represent transverse modes. (c) The effect of considering transverse elastic constant $C_T = 0.5$ [N m^{-1}]. The first band gap is closed and the others decrease as $\boldsymbol{\Omega} = 4$ [Hz].

$$
\begin{aligned}
L = & \sum_{m,n} \frac{M}{2}\left(\dot{\boldsymbol{\xi}}_{mn}^2 + \dot{\boldsymbol{\eta}}_{mn}^2\right) \\
& - \sum_{m,n} \frac{C_1}{2}\left\{\left[\hat{\mathbf{R}}_1 \cdot \left(\boldsymbol{\xi}_{mn} - \boldsymbol{\eta}_{mn}\right)\right]^2\right. \\
& + \left[\hat{\mathbf{R}}_2 \cdot \left(\boldsymbol{\xi}_{mn} - \boldsymbol{\eta}_{m-1,n}\right)\right]^2 \\
& \left. + \left[\hat{\mathbf{R}}_3 \cdot \left(\boldsymbol{\xi}_{mn} - \boldsymbol{\eta}_{m,n-1}\right)\right]^2\right\} \\
& - \sum_{m,n} \frac{C_2}{2}\left\{\left|\boldsymbol{\xi}_{mn} - \boldsymbol{\eta}_{mn}\right|^2\right. \\
& \left. + \left|\boldsymbol{\xi}_{mn} - \boldsymbol{\eta}_{m-1,n}\right|^2 + \left|\boldsymbol{\xi}_{mn} - \boldsymbol{\eta}_{m,n-1}\right|^2\right\},
\end{aligned}
\tag{A.2}
$$

where $C_1 = C_L - C_T$, $C_2 = C_T$. To focus on the effect of transverse restoring force, in (A.2) we neglect the terms resulted from rotation, i.e., the centrifugal and Coriolis terms. According to the Euler–Lagrange equation, the modified equations of motion are

$$
\begin{aligned}
\omega^2 \boldsymbol{\xi}_{mn} = & + \omega_1^2\left[\hat{\mathbf{R}}_1\hat{\mathbf{R}}_1 \cdot \left(\boldsymbol{\xi}_{mn} - \boldsymbol{\eta}_{mn}\right) + \hat{\mathbf{R}}_2\hat{\mathbf{R}}_2\right. \\
& \left. \cdot \left(\boldsymbol{\xi}_{mn} - \boldsymbol{\eta}_{m-1,n}\right) + \hat{\mathbf{R}}_3\hat{\mathbf{R}}_3 \cdot \left(\boldsymbol{\xi}_{mn} - \boldsymbol{\eta}_{m,n-1}\right)\right] \\
& + \omega_2^2\left[\left(\boldsymbol{\xi}_{mn} - \boldsymbol{\eta}_{mn}\right) + \left(\boldsymbol{\xi}_{mn} - \boldsymbol{\eta}_{m-1,n}\right)\right. \\
& \left. + \left(\boldsymbol{\xi}_{mn} - \boldsymbol{\eta}_{m,n-1}\right)\right] \\
\omega^2 \boldsymbol{\eta}_{mn} = & + \omega_1^2\left[\hat{\mathbf{R}}_1\hat{\mathbf{R}}_1 \cdot \left(\boldsymbol{\eta}_{mn} - \boldsymbol{\xi}_{mn}\right) + \hat{\mathbf{R}}_2\hat{\mathbf{R}}_2\right. \\
& \left. \cdot \left(\boldsymbol{\eta}_{m,n} - \boldsymbol{\xi}_{m+1,n}\right) + \hat{\mathbf{R}}_3\hat{\mathbf{R}}_3 \cdot \left(\boldsymbol{\eta}_{m,n} - \boldsymbol{\xi}_{m,n+1}\right)\right] \\
& + \omega_2^2\left[\left(\boldsymbol{\eta}_{mn} - \boldsymbol{\xi}_{mn}\right) + \left(\boldsymbol{\eta}_{m,n} - \boldsymbol{\xi}_{m+1,n}\right)\right. \\
& \left. + \left(\boldsymbol{\eta}_{m,n} - \boldsymbol{\xi}_{m,n+1}\right)\right]
\end{aligned}
\tag{A.3}
$$

and figures A1(a) and (b) indicate the band structure calculated from (A.3) with and without transverse elastic force. The light blue and blue line, respectively, correspond to optical and acoustic transverse mode, and the red and green lines represent the longitudinal modes. Thus, it is evident that the top and bottom band gradually evolve to flat bands as transverse elastic coefficient decreases. On the other hand, the transverse restoring force does not significantly affect the two longitudinal modes. Figure A1(c) illustrates the influence of transverse restoring force to zigzag edge modes. Band cross emerges for the first and second bands that close the band gap. For the second and third band gap, both gaps shrink when transverse elastic constant increases. Generally, for usual springs, the magnitude of the transverse elastic constant is much less than its longitudinal one. Therefore, negligence of the transverse restoring in our model should be considered as a reasonable approximation.

References

[1] von Klitzing K 1986 The quantized Hall effect *Rev. Mod. Phys.* **58** 519–31
[2] Hasan M Z and Kane C L 2010 Colloquium: topological insulators *Rev. Mod. Phys.* **82** 3045

[3] Qi X L and Zhang S C 2011 Topological insulators and superconductors *Rev. Mod. Phys.* **83** 1057
[4] Kane C L and Mele E J 2005 Quantum spin hall effect in graphene *Phys. Rev. Lett.* **95** 226801
[5] Bernevig B A, Hughes T L and Zhang S C 2006 Quantum spin hall effect and topological phase transition in HgTe quantum wells *Science* **314** 1757–61
[6] Haldane F D M 1988 Model for a quantum hall effect without Landau levels: condensed-matter realization of the 'parity anomaly' *Phys. Rev. Lett.* **61** 2015
[7] Raghu S and Haldane F D M 2008 Analogs of Quantum-hall-effect edge states in photonic crystals *Phys. Rev.* A **78** 033834
[8] Haldane F D M and Raghu S 2008 Possible realization of directional optical waveguides in photonic crystals with broken time-reversal symmetry *Phys. Rev. Lett.* **100** 013904
[9] Wang Z, Chong Y D, Joannopoulos J D and Soljačić M 2008 Reflection-free one-way edge modes in a gyromagnetic photonic crystal *Phys. Rev. Lett.* **100** 013905
[10] Ao X, Lin Z and Chan C T 2009 One-way edge mode in a magneto-optical honeycomb photonic crystal *Phys. Rev.* B **80** 033105
[11] Wang Z, Chong Y D, Joannopoulos J D and Soljačić M 2009 Observation of unidirectional backscattering-immune topological electromagnetic states *Nature* **461** 772–5
[12] Khanikaev A B, Mousavi S H, Tse W K, Kargarian M, MacDonald A H and Shvets G 2013 Photonic topological insulators *Nat. Mater.* **12** 233–9
[13] Rechtsman M C, Zeuner J M, Plotnik Y, Lumer Y, Podolsky D, Dreisow F, Nolte S, Segev M and Szameit A 2013 Photonic floquet topological insulators *Nature* **496** 196–200
[14] Torrent D and Sánchez-Dehesa J 2012 Acoustic analog of graphene: observation of Dirac cones in acoustic surface waves *Phys. Rev. Lett.* **108** 174301
[15] Torrent D, Mayou D and Sánchez-Dehesa J 2013 Elastic analog of graphene: Dirac cones and edge states for flexural waves in thin plates *Phys. Rev.* B **87** 115143
[16] Prodan E and Prodan C 2009 Topological phonon modes and their role in dynamic instability of microtubules *Phys. Rev. Lett.* **103** 248101
[17] Kane C L and Lubensky T C 2014 Topological boundary modes in isostatic lattices *Nat. Phys.* **10** 39
[18] Neto A C, Guinea F, Peres N M R, Novoselov K S and Geim A K 2009 The electronic properties of graphene *Rev. Mod. Phys.* **81** 109
[19] Cserti J and Tichy G 2004 A simple model for the vibrational modes in honeycomb lattices *Eur. J. Phys.* **25** 723
[20] Yan J A, Ruan W Y and Chou M Y 2008 Phonon dispersions and vibrational properties of monolayer, bilayer, and trilayer graphene: density-functional perturbation theory *Phys. Rev.* B **77** 125401
[21] Plotnik Y *et al* 2013 Observation of unconventional edge states in 'photonic graphene' *Nat. Mater.* **13** 57
[22] Savin A V and Kivshar Y S 2010 Vibrational Tamm states at the edges of graphene nanoribbons *Phys. Rev.* B **81** 165418
[23] Landau L D and Lifshitz E M 1976 Course of Theoretical Physics vol 1 *Mechanics* 3rd edn (Oxford: Butterworth-Heinemann)
[24] Kaliteevski M A, Beggs D M, Brand S, Abram R A and Nikolaev V V 2006 Statistics of the eigenmodes and optical properties of one-dimensional disordered photonic crystals *Phys. Rev.* E **73** 056616